Melt sustains pre-monsoon flow while groundwater drives the monsoon in the Nepal Himalayas

Non-peer reviewed preprint submitted to EarthArXiv

Luc Illien[1*], Christoff Andermann[2], Peter Makus[1], Niels Hovius[1]

[1]GFZ Helmholtz Centre for Geosciences, Potsdam, 14473, Germany

[2]Géosciences Rennes, Université de Rennes, CNRS, UMR 6118, Rennes, 35042, France

[*]Corresponding author. Email: lillien@gfz.de

Himalayan water-security assessments often focus on glacier retreat, yet groundwater may supply much of river flow. We combine seismic observations from the Hi-CLIMB transect across Nepal (2002–2004) with gauged discharge, satellite precipitation, and glacier-cover inventories to resolve when streamflow is sustained by melt versus groundwater. Relative seismic velocity changes track hillslope pore pressure and groundwater recharge, while river-induced seismic noise amplitudes provide a proxy for discharge variability along the Trisuli river. Unglaciated catchments show declining pre-monsoon discharge despite rainfall, consistent with subsurface moisture buffering and delayed runoff generation until monsoon groundwater recharge begins. In contrast, catchments with glacierized headwaters exhibit a pre-monsoon discharge rise attributable to melt, contributing an estimated 7% of annual discharge at a 20% glacier-cover outlet and sustaining river flow during the Spring season. During the monsoon, groundwater dominates runoff generation across elevations largely independent of glacier cover, with a sharp transition near 28.5°N consistent with monsoon penetration, highlighting high Himalayan "water towers" as groundwater-regulated systems with meltwater

acting as a critical seasonal buffer.

The Himalayan water towers of High Mountain Asia sustain freshwater supply, irrigated agriculture, and hydropower for more than 1.9 billion people across South Asia (*1, 2*). As atmospheric warming accelerates glacier retreat and water demand rises, the fate of Himalayan runoff has become a central climate-risk question (*3, 4*). Most assessments of future water security therefore emphasize glacier loss and declining meltwater contributions (*1, 4*). Yet Himalayan rivers are not supplied by ice alone. Increasing evidence indicates that groundwater contributes substantially to streamflow and may buffer discharge variability, implying that groundwater storage, rather than glacier ice alone, could become a primary control on hydrologic resilience in a warming Himalaya (*4–6*). Resolving this uncertainty requires identifying when and where precipitation contributes to groundwater recharge, a first-order control on water availability that remains poorly constrained in mountain catchments (*7*).

This uncertainty is especially acute in the Nepal Himalaya, where steep topography, monsoon seasonality, and large orographic gradients generate sharp contrasts in runoff processes and climate over short distances (*8, 9*). Despite the societal importance of Himalayan discharge, most assessments of hydrological transfers in High Mountain Asia rely on models, based on reanalyses of sparse observations, with much of the process understanding derived from the Tibetan Plateau (*6, 10*). Direct constraints from the heavily glacierized and snow-fed catchments of high-altitude catchments of Nepal remain limited. Large scale water budgets suggest that groundwater may account for a large fraction of annual discharge, in some basins approaching two-thirds of total runoff (*5, 6, 11*). Quantifying the relative importance of cryosphere melt and groundwater requires ground-based observations that span contrasting cryospheric settings, from the foreland Terai plains at the south, to the Tibetan plateau and the High Himalayas.

Here we leverage the Hi-CLIMB observational seismic array (Figure 1a), deployed across Nepal during 2002–2004, which provides an unusually dense transect (stations every 5-10 km on a 250 km distance) from the Terai foreland to the Tibetan Plateau, including major coverage within the Trisuli basin (*12*). We combine these records with seismic interferometry to track relative seismic velocity changes associated with hydrogeologic storage variations, and with seismic noise amplitudes as a proxy for river discharge dynamics (*13, 14*). By comparing glaciated and unglaciated catchments across the elevation gradient, and integrating independent discharge observations, satellite precipitation (*15*), and glacier-cover inventories (*16*), we resolve the seasonal timing of

groundwater recharge and runoff generation during a typical monsoon cycle. This framework allows us to quantify when cryosphere melt sustains streamflow and when groundwater becomes the dominant runoff source across the Nepal Himalaya.

Seismic observations resolve groundwater recharge and river discharge across a trans-Himalayan transect

Relative seismic velocity changes (dv/v) provide a sensitive proxy for seasonal groundwater storage dynamics, because increasing pore pressure and groundwater levels in porous rocks reduces seismic velocity (*17*). This hydrologic sensitivity has been demonstrated previously in Himalayan settings (*18, 19*), and the Hi-CLIMB transect reveals that the signal is strongly location dependent. Across the annual cycle, stations record distinct dv/v dynamics that vary with tectono-lithologic setting, topographic relief, and monsoon exposure, indicating that recharge and drainage processes are spatially heterogeneous across the Nepal Himalaya.

The strongest monsoon-season seismic velocity reductions occur in two zones (Figure 1c). The first lies along the southern Himalayan front near the Main Boundary Thrust (MBT), where steep topography rises abruptly from the sedimentary Terai plain and rainfall is intense. A second hotspot occurs farther north near the onset of the major topographic gradient around the Main Central Thrust (MCT), spanning the Lesser to Higher Himalaya. In both regions, monsoon precipitation is coincident with large seasonal decreases in seismic velocity, consistent with strong pore-pressure increases and groundwater recharge in fractured bedrock (*18*). By contrast, stations across the northern part of the transect, toward the Tibetan Plateau, show little or no monsoon-related velocity change, consistent with limited monsoon penetration into the rain-shadow domain (*8, 20*).

Two regions show muted seismic velocity variations despite monsoon rainfall: the Terai in the south and low-relief sedimentary basins between the recharge hotspots, including areas near Kathmandu. We interpret these weak seismic responses as lithologic storage effects rather than an absence of recharge. In these sedimentary deposits, high porosity and storage capacity may damp relative pore-pressure changes and reduce the seismic expression of recharge. In contrast, fractured crystalline rocks near the MBT and across the Lesser Himalaya likely experience larger seasonal pore-pressure variations because hydraulic heads can vary strongly over steep elevation gradients,

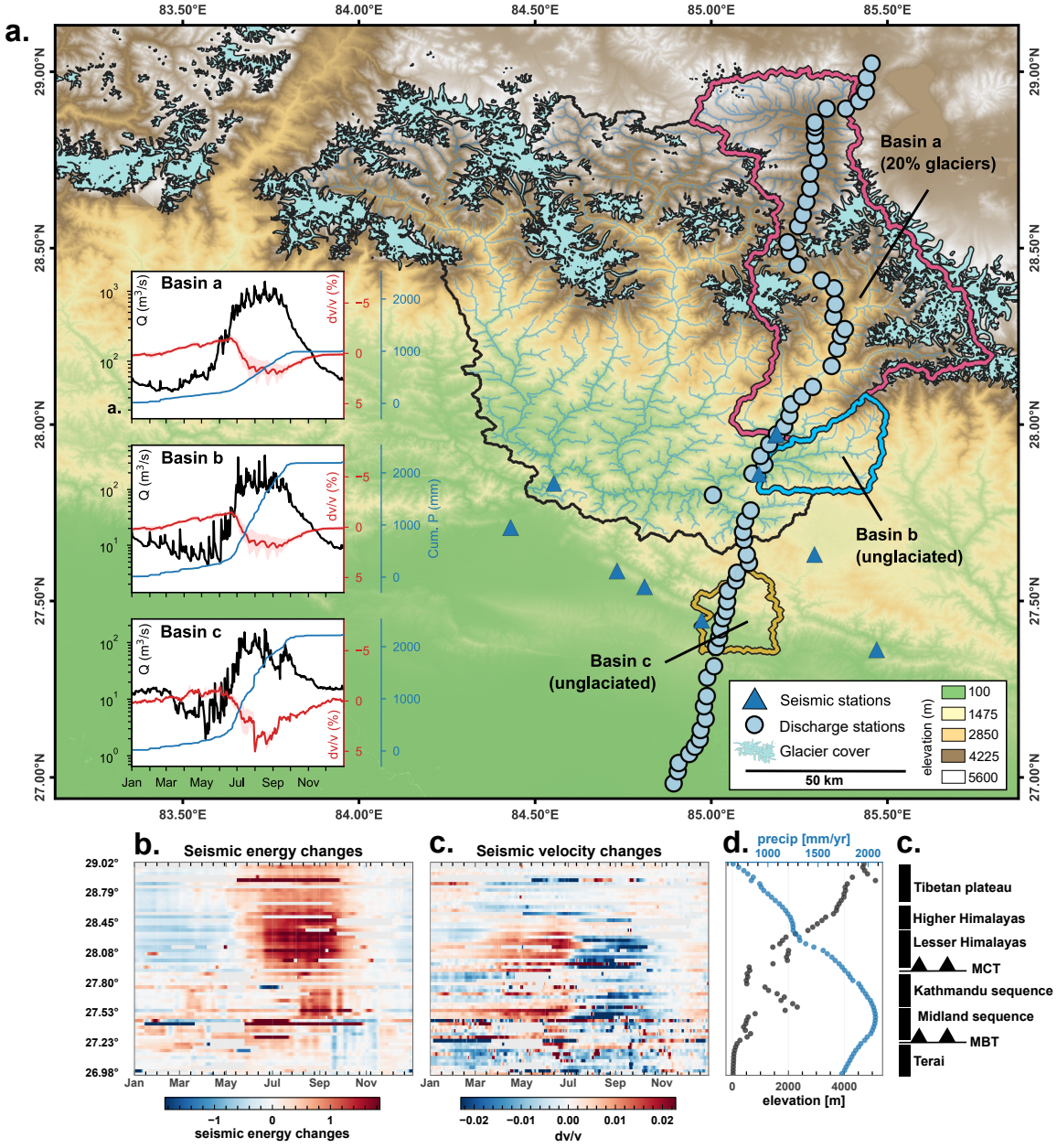

Figure 1: **Seismo-hydrologic observations across a trans-Himalayan transect in Nepal. (a)** Hi-CLIMB stations, discharge gauges, and analyzed catchments along the Trisuli system (basin *a*: upper Trisuli, ~20% glacier cover; basins *b,c*: unglaciated). Insets show daily discharge Q, relative seismic velocity change $\Delta v/v$, and cumulative precipitation. **(b)** River-induced seismic energy proxy (stations ordered by latitude). **(c)** Relative seismic velocity changes ($\Delta v/v$). **(d)** Latitudinal gradients in elevation and mean annual precipitation with major physiographic/tectonic domains and MBT/MCT.

amplifying the seismic response to recharge. Taken together, the seismic observations indicate that the most pronounced recharge occurs where high rainfall, steep topography, and fractured bedrock coincide.

At stations near the upper Trisuli trunk river (basin c in Figure 1a), seasonal changes in seismic noise amplitude are also pronounced and track river dynamics (Figure 1b), providing an independent proxy for discharge variability (*13*). The co-occurrence of discharge-related seismic energy variations and recharge-related velocity changes enables us to jointly assess groundwater storage and runoff generation across the transect. We therefore compare seismic records with precipitation and gauged discharge in representative unglaciated catchments (including catchments near the MBT and a tributary of the Trisuli) and in the upper Trisuli headwaters, where glacier cover is 20% (insets on Figure 1a).

This comparison reveals a sharp contrast in pre-monsoon runoff behavior. In unglaciated catchments, discharge continues to decline through the pre-monsoon period despite episodic rainfall, while seismic velocity increases, indicating that precipitation is not immediately converted to discharge but instead replenishes subsurface moisture storage. This pattern is consistent with recent field evidence from central Nepal, ~ 50km away, showing that early pre-monsoon rainfall is buffered by unsaturated soils and does not efficiently increase baseflow or trigger substantial groundwater recharge (*18*). Only later, when seismic velocity begins to decrease on stations located on draining slopes, does discharge rise rapidly with the monsoon. This onset is attributed to soil saturation. Before this recharge transition, discharge in these unglaciated basins remains low, at roughly 10% of monsoon peak flow in early June.

The glaciated upper Trisuli catchment shows a different seasonal dynamics. There, baseflow increases during the pre-monsoon, beginning around March, well before the onset of monsoon rainfall. We attribute this early rise in discharge to cryospheric melt generated upstream, as the timing coincides with the onset of seasonal snowmelt and with temperatures crossing 0°C in lower ablation zones (Figure S1). In the upper Trisuli, in June, pre-monsoon discharge reaches ~30% of monsoon peak flow, compared with only ~10% in unglaciated catchments. These observations show that cryosphere melt sustains river flow during the critical spring and pre-monsoon period, when runoff in unglaciated catchments is still largely buffered by subsurface moisture storage.

Melt provides a small but consequential share of discharge during the pre-monsoon season

The hydro–seismic comparisons above indicate that, in unglaciated basins, pre-monsoon precipitation is largely buffered in the subsurface and does not translate efficiently into streamflow until monsoon recharge thresholds are reached. This buffering implies that any sustained increase in pre-monsoon discharge in glacierized catchments is unlikely to be explained by rainfall alone, and instead points to a distinct water source that is available before the onset of widespread groundwater recharge. We therefore quantify how glacier cover modulates pre-monsoon runoff by comparing discharge dynamics along the Trisuli main stem (basin a in Figure 1) to those of a nearby unglaciated Trisuli tributary (basin b in Figure 1), using runoff ratios and precipitation-normalized discharge comparison.

Runoff ratios (Q/P) along the Trisuli exhibit their largest divergence during the pre-monsoon season (Figure 2a), while showing an increasing co-evolution during the monsoon from July to October. Because glacier cover decreases downstream due to lower-elevation and the progressive incorporation of non-cryospheric sub-basins, the distinct cyospheric pre-monsoon signal becomes increasingly diluted downstream and the runoff-ratio time-series approaches that of the unglaciated tributary.

To isolate seasonal discharge excesses not explained by precipitation differences and due to cryospheric input, we evaluate a precipitation-normalized discharge amplification factor that compares the ratio of discharge between the glacierized upper Trisuli and the unglaciated tributary to the ratio of their annual precipitation totals (Figure 2bc, Materials and Methods). Values near unity indicate that discharge differences are broadly consistent with precipitation scaling, whereas departures from unity indicate that the discharge ratio is amplified or damped relative to precipitation-based expectations. Across most of the year, this factor remains approximately constant and slightly above unity, which we attribute to higher evapotranspiration in the unglaciated basin due to lower elevation and latitude. However, during pre-monsoon, the factor rises, indicating that the glacierized outlet delivers more discharge than expected from precipitation scaling alone during this period. We note that using the same discharge ratio, but comparing both unglaciated catchments (the Trisuli tributary with the small catchment at the south), no deviation during pre-monsoon was observed.

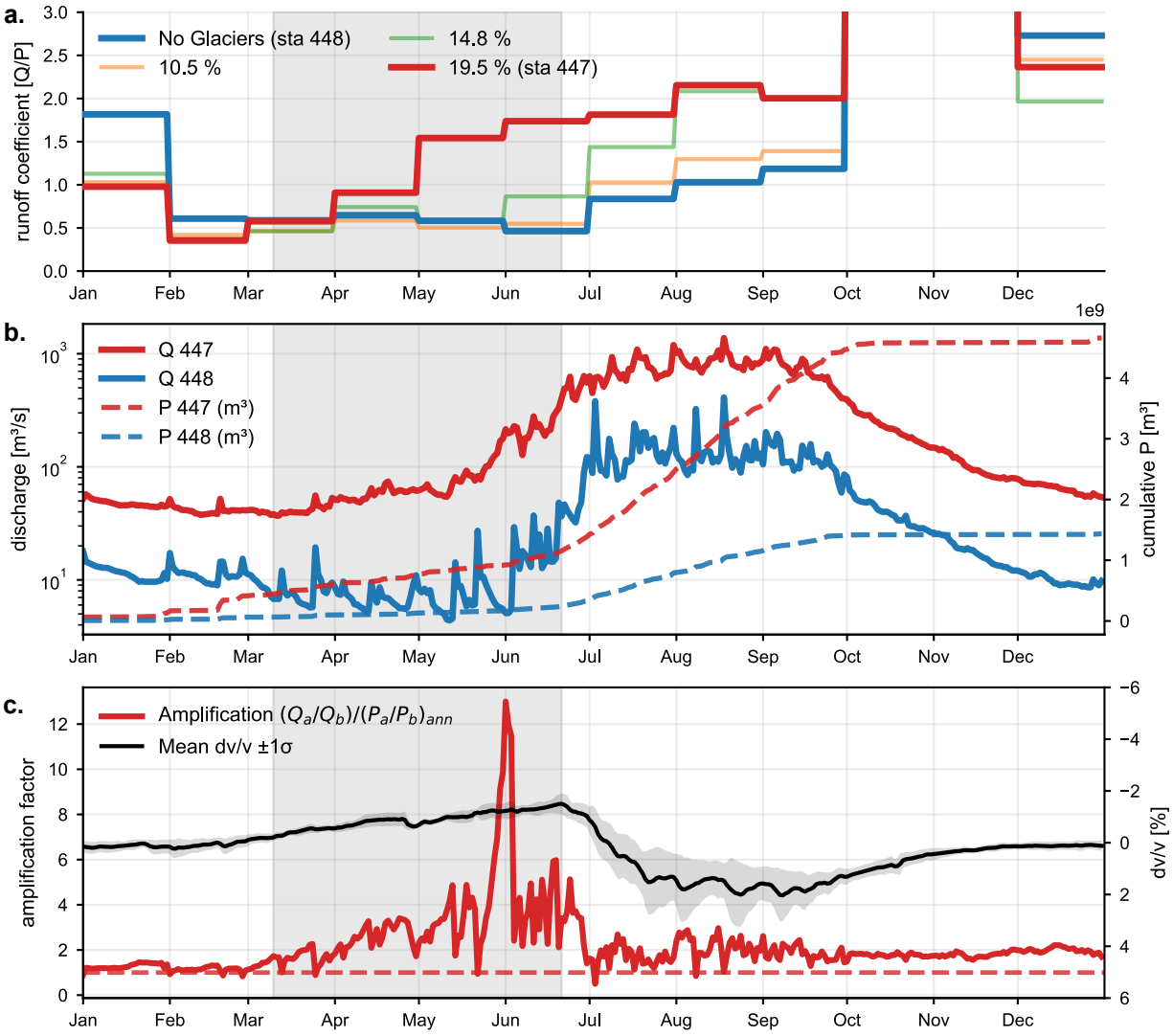

Figure 2: **Pre-monsoon melt amplifies discharge in glacierized headwaters, whereas monsoon flow is groundwater-dominated.** **(a)** Monthly runoff coefficient (Q/P) for nested Trisuli outlets spanning glacier cover from 0% (sta 448) to ~20% (sta 447); intermediate outlets are labelled by glacierized area fraction (10.5% and 14.8%). **(b)** Daily discharge at the glacierized outlet (Q447, red) and unglaciated outlet (Q448, blue) with cumulative precipitation (dashed; right axis; basin-integrated precipitation volume where available). **(c)** Precipitation-normalized discharge amplification factor $F(t) = (Q_a/Q_b)/(P_a/P_b)_{\text{ann}}$ (red), where $F = 1$ indicates discharge scaling consistent with the annual precipitation ratio; the mean seismic velocity proxy (black) indicates hillslope pressurization/recharge during the monsoon. Shading denotes the pre-monsoon analysis window used to assess excess discharge at the glacierized outlet.

Another feature is that the amplification factor collapses back toward its baseline value during the monsoon, coincident with the onset of groundwater recharge inferred from the drop in seismic velocity along the stations along the Trisuli. The convergence during the monsoon suggests that, once the landscape transitions into recharge, both basins are supplied predominantly by similar sources and pathways, with groundwater becoming the dominant contributor to streamflow regardless of glacier cover.

We use the pre-monsoon amplification to estimate an upper bound on the annual discharge fraction associated with cryospheric melt at the Upper Trisuli outlet. Specifically, we compute the time-integrated difference between observed discharge at the glacierized outlet and the discharge expected if it simply scaled with precipitation relative to the unglaciated outlet, and we express this excess volume as a fraction of the glacierized outlet's total annual discharged volume (Materials and Methods). We find that for the upper Trisuli, the pre-monsoon excess corresponds to approximately ∼7% of the total annual discharge. Because this estimate attributes all precipitation-normalized excess to cryospheric sources, it should be interpreted as an upper bound; lower evapotranspiration at higher elevations and other systematic basin differences would reduce the fraction that can be uniquely assigned to melt.

Although modest in the annual water budget, this melt-associated contribution occurs during the hydrologically critical spring and pre-monsoon season, when discharge in unglaciated basins remains strongly suppressed by subsurface moisture buffering. Cryosphere melt therefore provides an important support to river flow at the time of year when rainfall is least efficiently converted into runoff. Continued glacier retreat would be expected to diminish this pre-monsoon supply and amplify seasonal water stress in catchments with glacier-fed headwaters.

Groundwater dynamics dominates monsoon-driven flow across elevations

The ability to constrain hydrological processes and pathways across the Himalaya is often limited by the scarcity and uneven distribution of discharge gauges. Here, the seismic network provides a complementary constraint: stations along the upper Trisuli record strong seasonal variations in seismic noise amplitude driven by river activity (*13*), enabling us to track relative discharge dynamics continuously along the transect. At the gauge station (447), river-induced seismic amplitudes

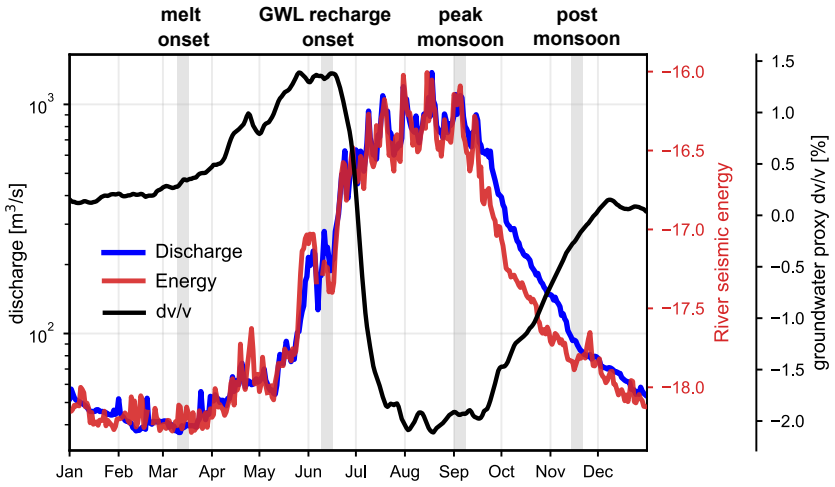

Figure 3: **Seismic river energy tracks discharge and brackets the seasonal transition to groundwater recharge.** Daily discharge (blue) and river-induced seismic energy (red; right axis) at the Trisuli outlet compared with relative seismic velocity changes (black; dv/v, right axis), interpreted as a proxy for hillslope pressurization and groundwater storage dynamics. Grey bands indicate key hydrologic phases: melt onset, groundwater-level (GWL) recharge onset, peak monsoon, and post-monsoon recession. Seismic energy closely follows discharge through the monsoon rise and peak, while dv/v decreases sharply at recharge onset and recovers during the post-monsoon recession, linking monsoon runoff generation and recession to groundwater dynamics.

closely covary with measured discharge (Figure 3), with episodic deviations likely associated with changes in sediment transport (*14, 21*). Leveraging this relationship, we use normalized seismic energy amplitudes as a proxy for river discharge variability along the Trisuli trunk using the seismic stations from 1000 m to 4000 m elevation, and interpret these variations together with the co-located seismic velocity changes that reflect local groundwater storage and recharge dynamics at the station.

To examine how runoff dynamics vary with cryospheric influence and climate forcing, we associate each station with a projected location on the Trisuli trunk and extract the upstream glacierized area fraction and catchment-integrated annual precipitation (annual mean precipitation multiplied by drainage area, Figure S2). We normalize seismic energy at each station by its annual maximum, such that values represent the fraction of peak river-induced energy ("relative peak energy") and are comparable across sites. We then extract seismic velocity and energy at four

reference periods that capture key phases of the hydrologic year (Figure 3): early March (onset of pre-monsoon melt at the Trisuli outlet), early June (late pre-monsoon, prior to widespread groundwater recharge inferred from seismic velocity), early September (monsoon peak discharge), and mid-November (post-monsoon recession and onset of freezing at high elevations).

In early March, most stations indicate relative river energy of ~10–30% of the annual peak, consistent with subdued dry-season flow (Figure 4). The exception occurs at the northern end of the transect on the Tibetan Plateau, where relative energy is higher (~40–50%), suggesting a more persistent cold-season contribution. By early June, stations south of ~28.5°N (elevation ~ 3900 m) show a coherent rise in relative river energy to ~20–40%, consistent with the pre-monsoon increase in discharge documented at the upper Trisuli gauge. During this same interval, seismic velocity changes increased, consistent with declining pore pressure and drainage of groundwater storage rather than recharge. This co-evolution in energy and velocity indicates that discharge increase in the Trisuli is not coupled to groundwater recharge and may instead be sustained by cryospheric inputs under weaker monsoon influence. Interestingly, the discharge signal at these higher latitudes does not coincide with the seismic signature of recharge (velocity reductions), suggesting that meltwater contributions are not accompanied by groundwater recharge at the scales sensed by the seismic stations.

At the peak of monsoon, river-energy amplitudes at all stations reach their annual maxima. South of ~28.5°N, seismic velocities decrease sharply during this period, and the largest velocity reductions coincide with the largest increases in relative river energy, particularly south of ~28.3°N. This covariation links peak monsoon runoff to increased pore pressure and widespread groundwater recharge and connectivity, indicating that groundwater becomes the dominant supplier of streamflow during monsoon conditions across latitudes and elevations along the stream. Following monsoon retreat, river energy declines at all sites, consistent with recession, while seismic velocities recover toward pre-monsoon values, implying that post-monsoon discharge is governed by groundwater drainage dynamics.

Three patterns emerge. First, across the set of stations influenced by the monsoon, the seasonal evolution of river-energy amplitudes and velocity changes is broadly similar despite glacier cover fractions ranging from ~5–20%, indicating that glacier cover is not a first-order control on monsoon runoff generation in this range. Second, the transect reveals a sharp transition in behavior near

~28.5°N (~ 3900m elevation), consistent with a strong orographic gradient in monsoon penetration that partitions a monsoon-coupled regime to the south from a more weakly monsoon-influenced regime to the north. Third, stations on the Tibetan Plateau show reduced annual variability in both river energy and seismic velocities, consistent with a comparatively resilient runoff contribution sustained by cold-season snow and melt inputs, in contrast to the strongly seasonal monsoon-driven regime at lower latitudes where dry-season flow remains a small fraction of peak discharge, driving even in glacier-influenced headwaters.

The intra-annual sensitivity of the mountain water towers

Our results shows that the Himalayan "water tower" is a seasonally-dependent system in which the dominant control on streamflow alternates between cryospheric inputs and groundwater storage and connectivity. In the Nepal Himalaya, meltwater acts primarily as a temporal buffer: it sustains river flow during spring and the pre-monsoon, when precipitation is preferentially absorbed into subsurface moisture reservoirs and runoff remains strongly suppressed in unglaciated catchments. With monsoon onset, however, discharge across elevations is generated predominantly by groundwater recharge and release, as indicated by the coherent coupling between river-induced seismic energy and seismic velocity reductions associated with pore pressure increase. In this sense, the resilience of these water towers is governed not only by the volume of stored ice, but by the timing and efficiency with which precipitation is transformed into groundwater and subsequently routed to channels.

This seasonal perspective also clarifies why glacier loss will not affect all users equally. For large rivers draining the Himalaya, glacierized area typically becomes a small fraction of total contributing area downstream (Figure S3) as catchments integrate lower-elevation, non-cryospheric terrain toward the Terai, where population density and water demand are highest. Consequently, meltwater may represent a limited component of annual discharge at basin outlets relevant to much of the downstream water budget. Yet for high-elevation communities and headwater users, the timing of melt contributions can be critical: even a modest annual fraction can provide a disproportionately important pre-monsoon supply when rainfall is least efficiently converted into runoff. In these settings, glacier and seasonal snow melt can sustain streamflow and water availability through the

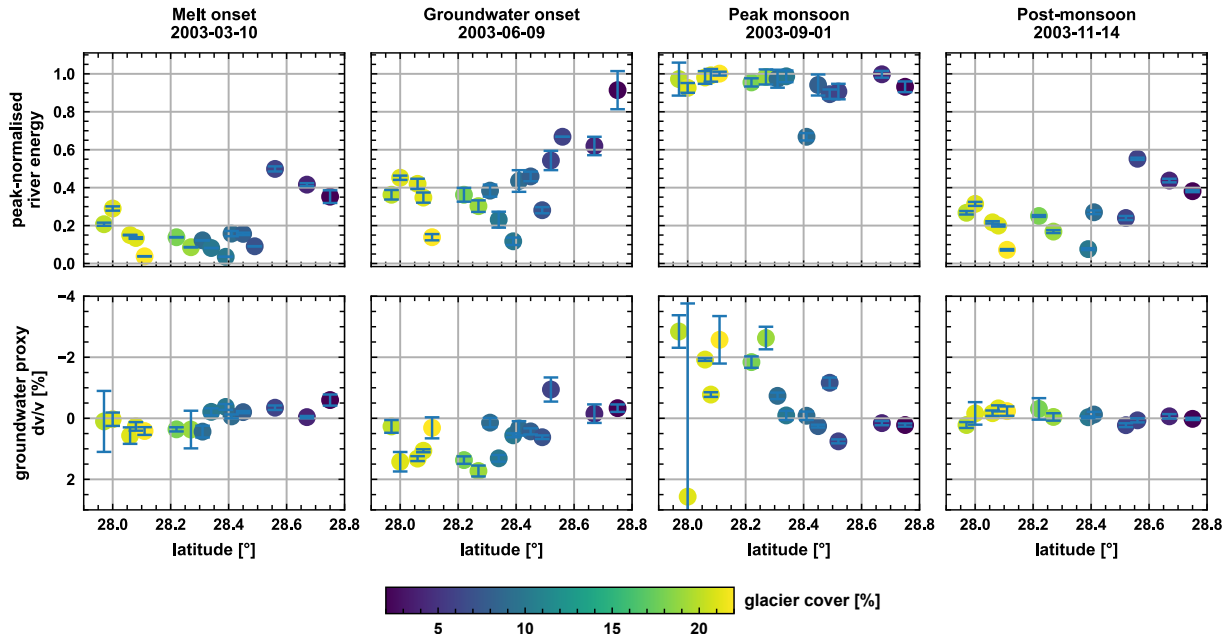

Figure 4: **Seasonal coherence of river discharge and groundwater recharge across the transect, and weak dependence on glacier cover.** Stations are summarized at four reference periods spanning the hydrologic year (columns; melt onset, groundwater recharge onset, peak monsoon, and post-monsoon recession; dates shown). **Top row:** peak-normalized river energy (seismic noise amplitude proxy for discharge) plotted against station latitude. **Bottom row:** groundwater proxy from relative seismic velocity changes (dv/v; sign consistent with pressurization/recharge during the monsoon) plotted against latitude. Marker color indicates upstream glacier cover fraction (5–20%). River energy increases from spring to peak monsoon across all latitudes south of ~28.5°N, coincident with a strong groundwater-recharge signal, whereas stations north of ~28.5°N show muted seasonal groundwater variability. Across the sampled range of glacier cover, seasonal patterns are broadly similar, indicating that monsoon runoff generation is primarily controlled by groundwater dynamics and monsoon penetration rather than glacier fraction.

dry season window when unglaciated catchments remain buffered by subsurface storage.

Looking forward, our findings suggest that a primary climate-change sensitivity of Himalayan water towers may arise through changes in precipitation seasonality and event structure, rather than through glacier retreat alone (*22*). If pre-monsoon precipitation increases (*23*), shifts toward higher intensity, or arrives earlier, the timing of the storage-to-runoff transition may change, potentially advancing or delaying the onset of widespread groundwater recharge and monsoon runoff generation. Because this transition is mediated by buffering in the unsaturated zone and the moisture threshold needed for groundwater connectivity, even subtle shifts in precipitation distribution could produce nonlinear changes in discharge timing. The combined effects of cryosphere decline (reducing pre-monsoon supply) and altered precipitation seasonality (modulating recharge onset and recession) therefore introduce substantial uncertainty into forecasts of future streamflow and water stress. These interactions motivate a broader emphasis on groundwater dynamics, particularly on recharge thresholds and storage, for assessments of Himalayan vulnerability and adaptation.

Reducing this uncertainty will require more direct constraints at high elevation, where the strongest gradients in monsoon penetration, snow processes, and glacier melt occur. Expanded monitoring of discharge, precipitation phase and intensity, snow storage, and meltwater generation in glacierized headwaters is essential for quantifying how sharp orographic transitions organize recharge and runoff (*9*). Although these high-elevation dynamics may represent a modest share of total annual water budgets at large downstream outlets, they can be vital for local water security and for anticipating other consequences: the co-evolution of glacier retreat and seasonal saturation states influences not only freshwater availability but also hazard potential, including the conditions that govern glacier-lake filling, drainage pathways, and the likelihood and impacts of glacial lake outburst floods (GLOFs) (*24*). Together, these needs argue for an expanded observational and modeling focus on groundwater as an integral component of the Himalayan water tower, linking climate forcing to both water resources and mountain hazards.

References and Notes

1. W. W. Immerzeel, *et al.*, Importance and vulnerability of the world's water towers. *Nature* **577** (7790), 364–369 (2020), doi:10.1038/s41586-019-1822-y, http://dx.doi.org/10.1038/s41586-019-1822-y.

2. D. Viviroli, M. Kummu, M. Meybeck, M. Kallio, Y. Wada, Increasing dependence of lowland populations on mountain water resources. *Nature Sustainability* **3** (11), 917–928 (2020), doi:10.1038/s41893-020-0559-9, http://dx.doi.org/10.1038/s41893-020-0559-9.

3. R. Ahmed, Decoding the Fate of Himalayan Glaciers under Climate Change: Impacts, Challenges, Research Gaps, and Policy Pathways. *Evolving Earth* **3**, 100082 (2025), doi:10.1016/j.eve.2025.100082, https://doi.org/10.1016/j.eve.2025.100082.

4. M. van Tiel, *et al.*, Cryosphere–groundwater connectivity is a missing link in the mountain water cycle. *Nature Water* **2** (7), 624–637 (2024), doi:10.1038/s44221-024-00277-8, http://dx.doi.org/10.1038/s44221-024-00277-8.

5. C. Andermann, *et al.*, Impact of transient groundwater storage on the discharge of Himalayan rivers. *Nature Geoscience* (5) (2012), doi:10.1038/NGEO1356, https://hal.archives-ouvertes.fr/hal-00710433.

6. Y. Yao, *et al.*, Role of Groundwater in Sustaining Northern Himalayan Rivers. *Geophysical Research Letters* **48** (10), 1–10 (2021), doi:10.1029/2020GL092354.

7. S. Gnann, *et al.*, The Influence of Topography on the Global Terrestrial Water Cycle. *Reviews of Geophysics* **63** (1), e2023RG000810, doi:https://doi.org/10.1029/2023RG000810.

8. B. Bookhagen, D. W. Burbank, Toward a complete Himalayan hydrological budget: Spatiotemporal distribution of snowmelt and rainfall and their impact on river discharge. *Journal of Geophysical Research: Earth Surface* **115** (F3) (2010), doi:https://doi.org/10.1029/2009JF001426, https://agupubs.onlinelibrary.wiley.com/doi/abs/10.1029/2009JF001426.

9. T. Biget, *et al.*, Brief communication: Sharp precipitation gradient on the southern edge of the Tibetan Plateau during cold season. *The Cryosphere* **19**, 5863–5870 (2025), doi:10.5194/tc-19-5863-2025, https://doi.org/10.5194/tc-19-5863-2025.

10. Y. Nan, *et al.*, Glacier meltwater has limited contributions to the total runoff in the major rivers draining the Tibetan Plateau. *npj Climate and Atmospheric Science* **8** (1), 155 (2025), doi:10.1038/s41612-025-01060-6, https://doi.org/10.1038/s41612-025-01060-6.

11. A. H. Schmidt, S. Lüdtke, C. Andermann, Multiple measures of monsoon-controlled water storage in Asia. *Earth and Planetary Science Letters* **546**, 116415 (2020), doi:10.1016/j.epsl.2020.116415, https://doi.org/10.1016/j.epsl.2020.116415.

12. John Nabelek, Collaborative Research: Lithospheric Scale Dynamics of Active Mountain Building along the Himalayan-Tibetan Collision Zone (2002), doi:10.7914/SN/XF_2002, https://www.fdsn.org/networks/detail/XF_2002/.

13. A. Burtin, L. Bollinger, J. Vergne, R. Cattin, J. L. Nábělek, Spectral analysis of seismic noise induced by rivers: A new tool to monitor spatiotemporal changes in stream hydrodynamics. *Journal of Geophysical Research: Solid Earth* **113** (B5) (2008), doi:https://doi.org/10.1029/2007JB005034, https://agupubs.onlinelibrary.wiley.com/doi/abs/10.1029/2007JB005034.

14. F. Gimbert, V. C. Tsai, M. P. Lamb, A physical model for seismic noise generation by turbulent flow in rivers. *Journal of Geophysical Research: Earth Surface* **119** (10), 2209–2238 (2014), doi:https://doi.org/10.1002/2014JF003201, https://agupubs.onlinelibrary.wiley.com/doi/abs/10.1002/2014JF003201.

15. G. Huffman, *et al.*, Integrated Multi-satellitE Retrievals for GPM (IMERG), Version 4.4, ftp://arthurhou.pps.eosdis.nasa.gov/gpmdata/ (2014), accessed 31 March 2015.

16. RGI 7.0 Consortium, Randolph Glacier Inventory - A Dataset of Global Glacier Outlines, Version 7.0 (2023), doi:10.5067/F6JMOVY5NAVZ, https://doi.org/10.5067/f6jmovy5navz.

17. M. A. Denolle, *et al.*, Ambient field seismology in critical zone hydrological sciences. *Comptes Rendus. Géoscience* **357**, 425–451 (2025), doi:10.5802/crgeos.310.

18. L. Illien, *et al.*, Subsurface Moisture Regulates Himalayan Groundwater Storage and Discharge. *AGU Advances* **2** (2) (2021), doi:10.1029/2021av000398.

19. L. Illien, *et al.*, Seismic Velocity Recovery in the Subsurface: Transient Damage and Groundwater Drainage Following the 2015 Gorkha Earthquake, Nepal. *Journal of Geophysical Research: Solid Earth* **127** (2), 1–18 (2022), doi:10.1029/2021jb023402.

20. B. Bookhagen, D. W. Burbank, Topography, relief, and TRMM-derived rainfall variations along the Himalaya. *Geophysical Research Letters* **33** (8) (2006), doi:https://doi.org/10.1029/2006GL026037, https://agupubs.onlinelibrary.wiley.com/doi/abs/10.1029/2006GL026037.

21. V. C. Tsai, B. Minchew, M. P. Lamb, J.-P. Ampuero, A physical model for seismic noise generation from sediment transport in rivers. *Geophysical Research Letters* **39** (2) (2012), doi:https://doi.org/10.1029/2011GL050255, https://agupubs.onlinelibrary.wiley.com/doi/abs/10.1029/2011GL050255.

22. M. Bernat, *et al.*, Precipitation phase drives seasonal and decadal snowline changes in high mountain Asia. *Environmental Research Letters* **20** (6), 064039 (2025), doi:10.1088/1748-9326/adcf39.

23. C. F. Brunello, *et al.*, Annually resolved monsoon onset and withdrawal dates across the Himalayas derived from local precipitation statistics. *Geophysical Research Letters* (2020), doi:10.1029/2020GL088420, https://agupubs.onlinelibrary.wiley.com/doi/abs/10.1029/2020GL088420.

24. K. L. Cook, C. Andermann, F. Gimbert, B. R. Adhikari, N. Hovius, *Glacial lake outburst floods as drivers of fluvial erosion in the Himalaya*, Tech. rep., http://science.sciencemag.org/.

25. L. Illien, C. Sens-Schönfelder, K.-Y. Ke, Resolving Minute Temporal Seismic Velocity Changes Induced by Earthquake Damage: The More Stations, the Merrier? *Geophysical Journal International* **234** (1), 124–135 (2023), doi:10.1093/gji/ggad038.

26. M. Beyreuther, *et al.*, ObsPy: A Python Toolbox for Seismology. *Seismological Research Letters* **81** (3), 530–533 (2010), doi:10.1785/gssrl.81.3.530.

27. C. Sens-Schönfelder, U. Wegler, Passive Image Interferemetry and Seasonal Variations of Seismic Velocities at Merapi Volcano, Indonesia. *Geophysical Research Letters* **33** (21), 1–5 (2006), doi:10.1029/2006GL027797.

28. P. Makus, C. Sens-Schönfelder, SeisMIC - an Open Source Python Toolset to Compute Velocity Changes from Ambient Seismic Noise. *Seismica* **3** (1) (2024), doi:10.26443/seismica.v3i1.1099.

29. G. D. Bensen, *et al.*, Processing Seismic Ambient Noise Data to Obtain Reliable Broad-Band Surface Wave Dispersion Measurements. *Geophysical Journal International* **169** (3), 1239–1260 (2007), doi:10.1111/j.1365-246X.2007.03374.x.

30. A. Obermann, T. Planés, C. Hadziioannou, M. Campillo, Lapse-Time-Dependent Coda-Wave Depth Sensitivity to Local Velocity Perturbations in 3-D Heterogeneous Elastic Media. *Geophysical Journal International* **207** (1), 59–66 (2016), doi:10.1093/gji/ggw264.

31. P. Makus, *et al.*, Deciphering the Whisper of Volcanoes: Monitoring Velocity Changes at Kamchatka's Klyuchevskoy Group With Fluctuating Noise Fields. *Journal of Geophysical Research: Solid Earth* **128** (4), e2022JB025738 (2023), doi:10.1029/2022JB025738.

Supplementary Materials for

Melt sustains pre-monsoon flow while groundwater drives the monsoon in the Nepal Himalayas

Non-peer reviewed preprint submitted to EarthArXiv

Luc Illien*, Christoff Andermann, Peter Makus, Niels Hovius

*Corresponding author. Email: lillien@gfz.de

This PDF file includes:

Materials and Methods

Figures S1 to S3

Materials and Methods

1 Seismic analysis

Table S1: **The frequency bands, for which the seismic data are analysed.** Within these frequency bands, we estimate both the seismic power (see 1.1) and the seismic velocity change (see 1.2). f_1 and f_2 denote the low-pass and high-pass critical frequencies of the filter, respectively. In the paper we report the seismic velocity changes at 4-8Hz and the seismic energy at 2-4Hz.

f_1	f_2
0.25	0.5
0.5	1.0
1.0	2.0
2.0	4.0
4.0	8.0
2.0	20.0

1.1 Computation the Seismic Power

For each of the seismic stations, we compute a measure for the average horizontal power P_h, which we define similarly to (*25*). Prior to computing P_h, we preprocess each daily trace of the seismic data by removing their linear trend and imposing a Hann taper on the first and last 2.5% of the traces. Subsequently, we deconvolve the instrument response and obtain seismograms given in velocity units (i.e., $\frac{m}{s}$). Then we bandpass filter the data in the frequency bands provided in Table S1. For each of those frequency bands, we compute $P_h(t)$:

$$P_h(t) = \ln\left(\frac{\tilde{E(t)} + \tilde{N(t)}}{2}\right), \tag{S1}$$

where $\tilde{E(t)}$ and $\tilde{N(t)}$ are the envelopes of the two horizontal components of the seismogram. We compute the envelope by computing the square root of the sum of the squared amplitude of the

data and its squared Hilbert transform (*26*):

$$\tilde{x(t)} = \sqrt{x^2(t) + (H(x(t)))^2} \tag{S2}$$

To obtain a measure for each day n, we compute the arithmic mean of P_h per station:

$$P_h^{(t_n)} = \frac{1}{t_{n+1} - t_n} \int_{t=t_n}^{t_{n+1}} P_h(t) \mathrm{d}t \tag{S3}$$

Because seismic energy is caused by river turbulence and sediment transport, we plot in the paper the results at 2-4Hz. Higher frequencies range may incorporate more energy due to sediment transport.

1.2 Computation of seismic velocity changes

To obtain a seismic velocity change time series, $dv/v(t)$, we use the stretching technique as proposed by (*27*). In practice, all described steps are executed in the SeisMIC software suite (*28*).

First, we preprocess the daily seismic raw recordings: We detrend and taper the data, apply an anti-alias filter and decimate the data to a sampling rate of 50 Hz and apply an additional bandpass filter between 0.01 and 25 Hz. Thereafter, the daily traces are slices into one-hour-long chunks, again tapered by 2% on either side, detrended, and bandpass filtered in the octave bands provided in Table S1. We avoid invasive non-linear preprocessing techniques such as spectral whitening or sign-bit-normalisation (*29*) and opt to merely mute the trace whenever its amplitude exceeds three times of its own standard deviation, thereby we mitigate the impact of sources with a strong directionality such as earthquakes.

For each frequency band, we compute hourly empirical Green's functions (EGFs) or correlation functions from autocorrelations and self-correlations (i.e., cross-correlations of the different components of a seismogram). To effectively exploit the stochastic properties of the ambient seismic field, we stack the hourly EGFs in per-day segments and smooth with a four-day-wide hanning window. The stretching technique requires the definition of a reference EGF, which defines the relativ measure of dv/v (i.e., the position of 0% velocity change). We choose this reference as the arithmetic mean of all EGFs retrieved from a specific component combination.

In essence, the stretching algorithm is a grid-search performed over a set of hypothetical homogeneous velocity changes for each time step. It stretches the time domain of the reference by a

stretching ratio ϵ and computes the Pearson correlation coefficient $\rho(t)$ between the EGF for each time step and the stretched references. $\hat{\epsilon}$, which yields the maximum correlation coefficient out of all tested values for ϵ, can then be used to infer a homogeneous velocity change $dv/v(t) = -\hat{\epsilon}(t)$. The time-series of the correlation coefficient $\rho(t)$ serves as a stability measure, effectively comparing the similarity between the stretched reference and each EGF, where $\rho = 1$ implies identity.

In practice, the stretching algorithm is perfomed on the coda of the correlation function to exploit the diffusive effect of scattering. Here, we choose to apply the algorithm between the lag times $\tau_1 = 4T$ and $\tau_2 = 12T$, where $T = \frac{1}{f_1}$ is the low pass period of each octave band. In this window, surface waves dominate the record, their maximum depth sensitivity is bounded at approximately two-thirds of the dominant wavelength (*30*). We test for velocity changes between -10 % and 10 %. The velocity change time series that we show in Figure 1c are station-wide means that we retrieved by averaging the posterior probability density functions returned by the stretching algorithm, the so-called similarity matrices, for all auto- and self-correlations of a single station (*31*).

Construction of seismic energy and velocity-change latitude matrices

To characterize the seasonal evolution of seismic wavefield properties across the network, we constructed station-by-day matrices of seismic energy and relative seismic velocity change (dv/v). In these matrices, each row corresponds to a seismic station and each column corresponds to a day of the year (DOY).

Seismic energy. For each station, we extracted the daily seismic envelope power within a predefined frequency band. The frequency band used in the analysis was selected by an index $f_{\min}$, corresponding to one of several precomputed spectral bands. Let $E_s(t)$ denote the daily seismic energy time series for station s at time t. Before seasonal stacking, spurious values were removed by excluding zero values and, where applicable, values outside predefined amplitude bounds. Short data gaps were filled by interpolation over a limited time span, and the resulting time series was smoothed using a moving window.

To isolate the seasonal component, the station-specific mean was removed from the smoothed energy series:

$$E'_s(t) = E_s(t) - \overline{E_s}, \tag{S4}$$

where $\overline{E_s}$ is the temporal mean of the smoothed series for station s.

The annual cycle was then constructed by grouping all observations according to their day of year. For each station s and each day of year d, the annual seismic energy was computed as the arithmetic mean of all available values associated with that calendar day:

$$\widetilde{E}_s(d) = \frac{1}{N_{s,d}} \sum_{i=1}^{N_{s,d}} E'_s(t_i), \tag{S5}$$

where $N_{s,d}$ is the number of valid observations for station s associated with day d across the full observation period. This procedure preserves single observations where only one valid sample exists for a given day of year.

To place all annual cycles on a common time axis, the climatological dates were mapped onto a reference year (2003), preserving month and day while removing interannual variability.

Relative seismic velocity change. Daily relative velocity changes, denoted $v_s(t)$, were obtained independently for each station using noise-based seismic monitoring. Each dv/v estimate was associated with a correlation coefficient $c_s(t)$, which quantifies the similarity between the daily waveform and the reference waveform used in the monitoring procedure. To reduce the influence of poorly constrained measurements, the annual cycle of dv/v was computed using a correlation-weighted average.

For each valid daily estimate, a weight was defined from the corresponding waveform correlation coefficient,

$$w_s(t) = c_s(t). \tag{S6}$$

The annual cycle of dv/v for station s and day of year d was then computed as

$$\widetilde{v}_s(d) = \frac{\sum_{i=1}^{N_{s,d}} w_s(t_i)\, v_s(t_i)}{\sum_{i=1}^{N_{s,d}} w_s(t_i)}. \tag{S7}$$

If the denominator was zero for a given day (for example, if all correlation coefficients were equal to zero), the weighted average was replaced by the unweighted mean:

$$\widetilde{v}_s(d) = \frac{1}{N_{s,d}} \sum_{i=1}^{N_{s,d}} v_s(t_i). \tag{S8}$$

To facilitate comparison among stations, we removed the mean dv/v over a predefined reference window:

$$\widetilde{v}'_s(d) = \widetilde{v}_s(d) - \langle \widetilde{v}_s(d) \rangle_{d \in \mathcal{W}}\,, \tag{S9}$$

where $\mathcal{W}$ denotes the selected reference interval in day-of-year space. This step highlights relative seasonal deviations rather than absolute offsets.

Matrix construction. The processed annual cycles were assembled into matrices in which rows correspond to stations and columns correspond to day of year (1–365). Specifically, we built:

1. an energy matrix **E** containing $\widetilde{E}_s(d)$,
2. a velocity-change matrix **V** containing $\widetilde{v}'_s(d)$,
3. a similarity matrix **C** containing $\widetilde{c}_s(d)$ or, alternatively, a decorrelation matrix **D** containing $\widetilde{D}_s(d)$.

Stations were arranged according to geographic metadata (e.g., latitude or elevation) to facilitate spatial interpretation. The resulting station-by-day matrices were visualized as two-dimensional color maps, allowing direct comparison of seasonal patterns in seismic energy, relative velocity change, and waveform decorrelation across the seismic network.

1.3 Amplification factor and excess discharge budget

To quantify deviations from precipitation-controlled discharge scaling between neighboring catchments, we define a *discharge-ratio amplification factor* that compares the observed discharge ratio to the ratio expected from basin-integrated precipitation.

Let $Q_a(t)$ and $Q_b(t)$ denote the mean daily discharge ($m^3\ s^{-1}$) measured at two outlet stations draining catchments a and b, respectively. Similarly, P_a and P_b denote the total precipitation integrated over each catchment during the study year. The amplification factor is defined as

$$F(t) = \frac{(Q_a/Q_b)(t)}{(P_a/P_b)_{\mathrm{ann}}}, \tag{S10}$$

where $(P_a/P_b)_{\mathrm{ann}}$ represents the ratio of total annual precipitation received by the two basins. In this formulation, $F = 1$ corresponds to the case where the discharge ratio follows the precipitation

ratio, while $F > 1$ ($F < 1$) indicates that catchment a produces proportionally more (less) discharge than expected from precipitation alone.

This metric provides a dimensionless measure of relative hydrologic amplification between the two basins. Because the precipitation ratio represents the long-term forcing contrast between the basins, deviations of $F(t)$ from unity reflect differences in hydrologic response, including storage release, connectivity changes, or delayed routing processes.

To quantify the volumetric impact of these deviations, we define a reference discharge for catchment a that corresponds to the precipitation-scaled expectation,

$$Q_{a,\mathrm{exp}}(t) = \left(\frac{P_a}{P_b}\right)_{\mathrm{ann}} Q_b(t). \tag{S11}$$

The instantaneous discharge anomaly is therefore

$$\Delta Q_a(t) = Q_a(t) - Q_{a,\mathrm{exp}}(t). \tag{S12}$$

Because discharge is measured as a mean daily flux, the corresponding excess water volume associated with this anomaly is obtained by integrating over time,

$$\Delta V = \sum_{t \in W} \left[Q_a(t) - Q_{a,\mathrm{exp}}(t)\right] \Delta t, \tag{S13}$$

where W denotes the analysis window (Fig. X), and $\Delta t = 86400$ s corresponds to one day. Positive values of ΔV represent additional discharge delivered by catchment a relative to the precipitation-scaled expectation, whereas negative values represent a deficit.

For comparison across basins and years, this excess volume is normalized by the total annual discharge volume of catchment a,

$$V_a = \sum_{\mathrm{year}} Q_a(t)\, \Delta t. \tag{S14}$$

The fractional excess discharge is then expressed as

$$\mathrm{Excess} = \frac{\Delta V}{V_a}. \tag{S15}$$

Applying this formulation to the analysis window highlighted in Fig. X yields an excess discharge corresponding to approximately 7% of the total annual discharge volume of catchment a. This value

represents the cumulative volume of water released in excess of the precipitation-scaled reference during the analyzed period.

Importantly, this estimate does not represent newly generated water but rather a relative discharge surplus with respect to the precipitation-based reference state. As such, the excess volume reflects hydrologic processes that temporarily enhance discharge in catchment a relative to catchment b, including transient storage release and changes in subsurface connectivity.

1.4 Extraction of basin-averaged precipitation from GPM and APHRODITE

To quantify precipitation forcing at each seismic station, we extracted basin-averaged precipitation time series from gridded precipitation products using the upstream catchment of each station as a spatial mask. For each seismic station, the upstream drainage area was delineated independently and exported as a polygon shapefile. This polygon therefore represents the basin contributing runoff to the station location.

The same extraction procedure was applied to both the GPM IMERG and APHRODITE precipitation datasets. First, the basin shapefile was read in MATLAB and its polygon coordinates were converted from geographic coordinates (longitude and latitude) into the index space of the precipitation grid. For the GPM product used here, the native grid resolution is $0.1^\circ \times 0.1^\circ$. Because the basin boundaries are generally not aligned with the precipitation grid, we refined the spatial mask by subdividing each precipitation pixel into smaller subcells. In the implementation, a computational resolution of 15 arc-seconds was used. The corresponding subcell size in degrees is

$$\Delta = \frac{15}{3600}^\circ,$$

so that each 0.1° precipitation pixel is subdivided into

$$N = \frac{0.1}{\Delta} \approx 24$$

subcells in each horizontal direction. Thus, each original precipitation pixel is represented by a 24×24 fine grid for mask construction.

A binary basin mask was then generated on this finer grid, with value 1 for subcells inside the basin polygon and 0 for subcells outside. For each day, the precipitation field was read from the gridded product and cropped to the bounding box of the basin. Each original precipitation grid cell

within this subset was expanded onto the finer grid by assigning its precipitation value uniformly to all associated subcells. The basin mask was then applied to retain only the subcells located within the upstream catchment. Basin-averaged precipitation was computed as the arithmetic mean of the precipitation values inside the mask:

$$\bar{P} = \frac{1}{N_b} \sum_{i=1}^{N_b} P_i,$$

where P_i is the precipitation assigned to subcell i and N_b is the total number of subcells inside the basin. This approach accounts for partial overlap between the catchment boundary and the precipitation pixels, and therefore provides a more accurate estimate of mean basin precipitation than a simple whole-pixel selection.

The extraction was repeated for every basin shapefile corresponding to the seismic stations and for every time step in the precipitation record. Daily basin-averaged precipitation was computed directly from the daily gridded fields. Monthly and annual precipitation were obtained by summing daily precipitation fields through time before applying the same basin mask and computing summary statistics. In addition to the mean precipitation, the standard deviation, minimum, and maximum values within each masked basin were also recorded. The resulting time series represent the mean precipitation forcing over the upstream area of each seismic station and were used for comparison with the seismic observations.

1.5 DEM and glacier cover analysis

Digital elevation model (DEM) analyses were performed to derive the hydrographic network and upstream drainage areas associated with seismic and hydrological stations. Topographic data were obtained from the Shuttle Radar Topography Mission (SRTM) DEM at 1-arc-second spatial resolution. Glacier outlines were imported as shapefiles from the Randolph Glacier Inventory (RGI).

The DEM was processed using a standard hydrographic workflow in QGIS. This included the derivation of flow direction and flow accumulation grids, from which the river network and main trunk were extracted. For each seismic station located close to the river, as well as for each discharge station, the station location was projected onto the main river trunk in order to define a consistent outlet point on the drainage network. Upstream catchments were then delineated from the DEM using these projected outlet locations.

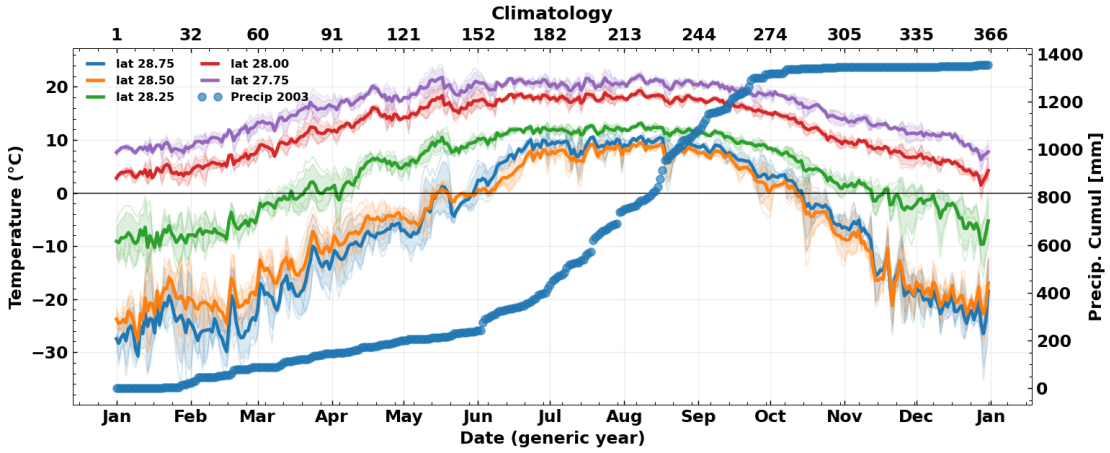

Figure S1: **Climatological temperature gradients and monsoon-season precipitation across the transect.** Daily mean 2-m air temperature from ERA5 (colored lines) for representative station groups along the Hi-CLIMB latitude transect (labels indicate station latitude); shaded envelopes show intra-seasonal variability. Blue circles show cumulative precipitation for 2003 (right axis). Temperatures cross 0°C earlier and remain positive longer at lower latitudes, while cumulative precipitation rises sharply during the monsoon (June–September), highlighting strong seasonality in melt potential and water inputs across the transect.

For each delineated catchment, the total upstream area was calculated from the basin shapefile. Glacier outlines were then intersected with the corresponding upstream basin polygon to quantify the glacierized area contained within that catchment. Glacier cover was finally expressed as the percentage of glacierized area relative to the total upstream drainage area:

$$G = \frac{A_{\text{glacier}}}{A_{\text{basin}}} \times 100, \tag{S16}$$

where A_{glacier} is the glacierized area within the upstream catchment and A_{basin} is the total upstream basin area.

This procedure provided an estimate of glacier cover for the catchments associated with each seismic station and discharge station.

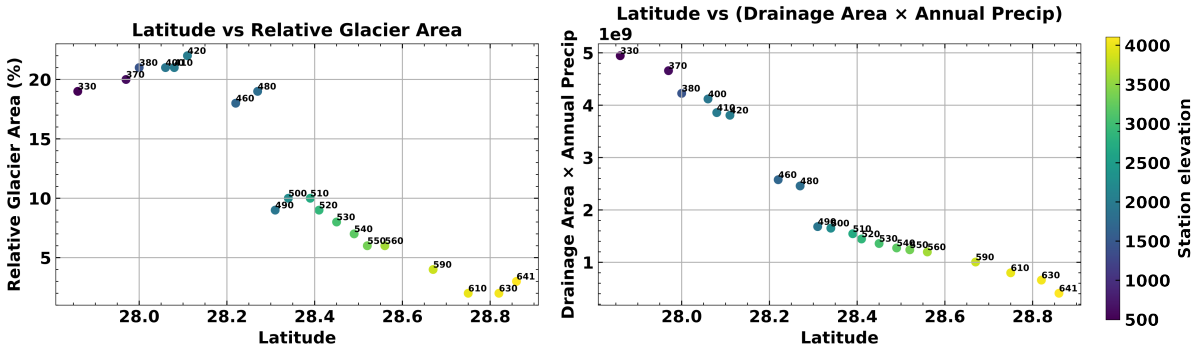

Figure S2: **Latitudinal gradients in cryospheric influence and precipitation forcing along the transect. Left:** Relative glacierized area fraction (%) for catchments associated with each seismic/discharge site plotted against latitude. **Right:** Catchment-integrated annual precipitation forcing, expressed as drainage area × mean annual precipitation, plotted against latitude. Point labels indicate station IDs; marker color encodes elevation (m; color bar). Together, the panels show a sharp northward decrease in precipitation forcing and glacier influence across the transect, consistent with strong orographic control on monsoon penetration and headwater cryosphere extent.

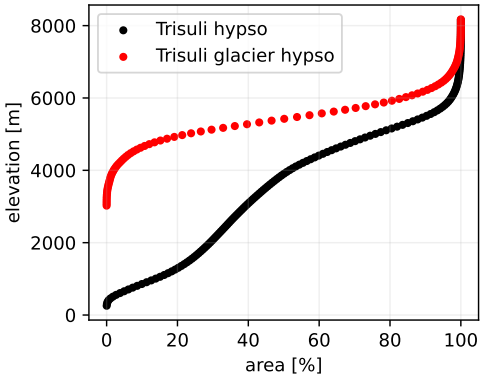

Figure S3: **Hypsometry of the Trisuli basin and its glacierized area.** Cumulative hypsometric curves showing the distribution of basin area with elevation for th entire Trisuli catchment (black) and for the glacierized fraction only (red, ~14% of the surface of the Trisuli). The glacier hypsometry is concentrated at high elevations (predominantly above ~4,500–5,000 m), whereas the total basin area spans a broad elevation range from the foreland to the highest headwaters, illustrating how cryospheric inputs originate from a limited, high-altitude portion of the catchment.